

Micromagnetic simulations on the grain shape effect in Nd-Fe-B magnets

Min Yi, Oliver Gutfleisch, and Bai-Xiang Xu

Citation: *Journal of Applied Physics* **120**, 033903 (2016); doi: 10.1063/1.4958697

View online: <http://dx.doi.org/10.1063/1.4958697>

View Table of Contents: <http://scitation.aip.org/content/aip/journal/jap/120/3?ver=pdfcov>

Published by the [AIP Publishing](#)

Articles you may be interested in

Micromagnetic simulation of the orientation dependence of grain boundary properties on the coercivity of Nd-Fe-B sintered magnets

AIP Advances **6**, 056028 (2016); 10.1063/1.4944773

Large-scale micromagnetic simulation of Nd-Fe-B sintered magnets with Dy-rich shell structures

AIP Advances **6**, 056006 (2016); 10.1063/1.4943058

Magnetism in grain-boundary phase of a NdFeB sintered magnet studied by spin-polarized scanning electron microscopy

Appl. Phys. Lett. **104**, 232408 (2014); 10.1063/1.4883487

Crystallographically anisotropic $\text{Sm}_2\text{Fe}_{17}\text{N}_6$ and $\text{Nd}(\text{Fe},\text{Mo})_{12}\text{N}$ x hard magnetic flakes

J. Appl. Phys. **115**, 17A711 (2014); 10.1063/1.4862849

Magnetic properties of Nd-Fe-B thick film magnets prepared by using arc deposition

J. Appl. Phys. **107**, 09A744 (2010); 10.1063/1.3348233

The new SR865 2 MHz Lock-In Amplifier ... \$7950



Chart recording



FFT displays



Trend analysis

Features

- Intuitive front-panel operation
- Touchscreen data display
- Save data & screen shots to USB flash drive
- Embedded web server and iOS app
- Synch multiple SR865s via 10 MHz timebase I/O
- View results on a TV or monitor (HDMI output)

Specs

- 1 MHz to 2 MHz
- 2.5 nV/√Hz input noise
- 1 μs to 30 ks time constants
- 1.25 MHz data streaming rate
- Sine out with DC offset
- GPIB, RS-232, Ethernet & USB

SRS Stanford Research Systems
www.thinkSRS.com · Tel: (408)744-9040

Micromagnetic simulations on the grain shape effect in Nd-Fe-B magnets

Min Yi,^{1,a)} Oliver Gutfleisch,^{1,2} and Bai-Xiang Xu¹

¹*Institute of Materials Science, Technische Universität Darmstadt, 64287 Darmstadt, Germany*

²*Fraunhofer IWKS Project Group for Materials Cycles and Resource Strategy, 63450 Hanau, Germany*

(Received 6 May 2016; accepted 28 June 2016; published online 18 July 2016)

Micromagnetic simulations were performed to study the effect of grain shape and defect layer in Nd-Fe-B magnets. It was found that the coercivity can be increased by a factor of ~ 2 by changing the grain shape from the triangular prism to the spheroid. Both the anisotropy field contribution and the shape contribution to the coercivity, and thus also the final coercivity, were found to decrease in the order: spheroid > circular prism > hexagonal prism > square prism > triangular prism. Sputtered columnar grains and hot-deformed platelet grains with a constant volume were also considered. Results show that the coercivity initially increases with the aspect ratio and then nearly saturates above the ratio of ~ 4 . Simulations of multigrain ensembles showed that depending on the grain shape, compared to the case of single grain, a further decrease of $\sim 10\%$ – 45% in the coercivity is induced by magnetostatic coupling. *Published by AIP Publishing.*

[<http://dx.doi.org/10.1063/1.4958697>]

I. INTRODUCTION

For hybrid electric vehicle and wind turbine generator applications, Nd-Fe-B based permanent magnets with high coercivity are required.^{1,2} Generally, there are two ways to increase the coercivity in Nd-Fe-B magnets. One way is to increase the magnetocrystalline anisotropy of the Nd₂Fe₁₄B phase by substituting Dy for a fraction of Nd atoms.^{3–5} But in the long term, the scarcity of Dy dejects the continued use of Dy in Nd₂Fe₁₄B magnets. The other way is to optimize the extrinsic properties by microstructural engineering such as grain boundary diffusion.^{2,6–8} The latter is currently widely studied, since it makes the utilization of Dy more efficient.

In turn, the reason why the coercivity of standard Nd-Fe-B magnets is far below that of the theoretical value is greatly attributed to the extrinsic microstructural features. In the modelling aspect of this issue, micromagnetic simulations^{9,10} and mechanically coupled phase-field simulations^{11–14} are two methods for studying the microscopic behavior of magnets. Especially, in view of the variability in microstructures, micromagnetic simulations^{9,10} have been the powerful tools for aiding experiments about exploring effects of grain size, grain boundary phase, and grain alignment. For example, Sepehri-Amin *et al.*¹⁵ and Liu *et al.*¹⁶ combined experiments and micromagnetic simulations to study the grain size dependence of coercivity in Nd-Fe-B magnets. Hrkac *et al.*^{17–19} investigated the effect of grain boundary composition on the coercivity of Nd-Fe-B grain ensembles by a combination of atomistic and micromagnetic simulations. Fujisaki *et al.*²⁰ used micromagnetic simulations to study the magnetization reversal in misaligned multigrain magnets.

As one critical microstructural parameter, grain shape, especially the edges or corners, can affect the local demagnetization field distribution and thus the local magnetic reversal

behavior.^{21–24} The premature nucleation of the locally reversed domain is unfavorable for an enhanced coercivity. Therefore, grain shape should play an important role on the coercivity, and it is also possible to tailor the grain shape to adjust the shape contribution to the coercivity. However, to the best of our knowledge, a systematic study on the grain shape effect in Nd-Fe-B is still meaningful according to the literatures. Bance *et al.*^{25–27} used the cubic or dodecahedral single grain covered by a defect layer to study the defect thickness dependent angular dependence of coercivity and the thermally activated coercivity in Nd-Fe-B by micromagnetic simulations. Based on the sub-micron Nd₂Fe₁₄B single and perfect grain with a rectangular prism shape, Thielsch *et al.*²³ applied micromagnetic simulations to reveal the dependence of coercivity on length ratios. Krone *et al.*²⁸ carried out micromagnetic simulations to study the magnetization reversal processes and energy barrier of single and perfect grain nanomagnets with rectangular prism and cylinder shapes. With respect to nanocomposite permanent magnets, Fischbacher *et al.*²⁹ used micromagnetic simulations to study the role of the size and shape of the soft inclusions on the magnetization reversal by considering magnetically soft spheroids, cuboids, and cylinders embedded in a hard magnetic matrix. More importantly, Bance *et al.*³⁰ performed micromagnetics of shape anisotropy based cylindrical and spheroidal magnets, but with the magnetocrystalline anisotropy ignored. With a focus on the grain-size dependent demagnetizing factors in permanent magnets, they also studied three different shapes (i.e., sphere, dodecahedron, and cube) which are all without any defects.²⁴ These relatively scattered studies with different focuses have provided fruitful information on the grain shape effect and its underlying mechanisms in Nd-Fe-B magnets. Based on these previous studies, in this work we consider the surface defects in the Nd-Fe-B single grain or multigrain. A systematic study was carried out for anatomizing the grain shape effect on the reversal process and coercivity in Nd-Fe-B magnets. The

^{a)}Electronic mail: yi@mfm.tu-darmstadt.de

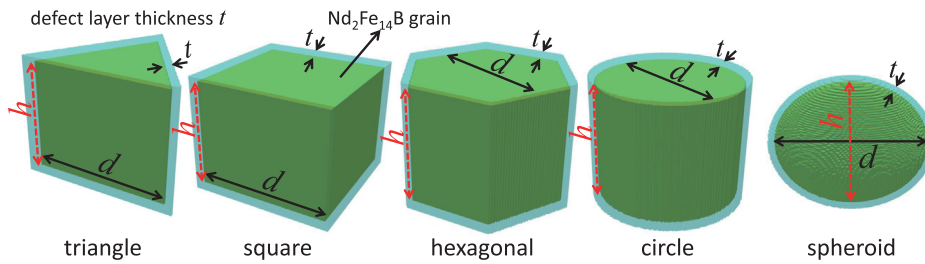


FIG. 1. Illustrated three-dimensional geometry of prisms and spheroid. The $\text{Nd}_2\text{Fe}_{14}\text{B}$ grain is covered by a defect layer with a thickness of t . For the prisms, the height of $\text{Nd}_2\text{Fe}_{14}\text{B}$ grain is h , with a cross-section size of d . For the spheroid, the equatorial diameter is d and the size in the polar direction is h . The easy axis is along the height (prisms) or polar (spheroid) h direction.

spheroid grain and the prism grain with triangular, rectangular, hexagonal, and circular cross sections were taken into account. The platelet grains motivated by the hot-deformed Nd-Fe-B magnets and the columnar grains motivated by the sputtered Nd-Fe-B magnets were also studied.

II. SIMULATION DETAILS

The three-dimensional geometry of the prisms and spheroid used for simulations is illustrated in Fig. 1. The height of the prism grain is set as h , with a cross-section geometry d . The spheroid grain is with an equatorial diameter of d and a polar diameter of h . The easy axis is along the height (prisms) or polar (spheroid) h direction. Recent atomistic simulations have shown that the $\text{Nd}_2\text{Fe}_{14}\text{B}$ grain surface or edges are covered by a defect layer due to the local strain near the grain boundary or interfaces.^{17–19} The grain boundary phase itself can also be a soft magnetic material.³¹ So we set a defect layer with a thickness of t around the grain surface. The defect thickness t is varied from 1 to 10 nm. For the case of varied aspect ratio h/d , d^2h is kept constant as $2 \times 10^6 \text{ nm}^3$. h is changed from 22 to 556 nm, while d from 60 to 300 nm which is around the critical size of single-domain particles.^{32,33} Material parameters for $\text{Nd}_2\text{Fe}_{14}\text{B}$ grain at room temperature were obtained from the literature¹⁵ as magnetocrystalline anisotropy: $K = 4.5 \text{ MJ/m}^3$, saturation magnetization $\mu_0 M_s = 1.61 \text{ T}$, and exchange constant $A = 12.5 \text{ pJ/m}$. The magnetic property of the defect layer is chosen the same as that of $\text{Nd}_2\text{Fe}_{14}\text{B}$ grain, but with zero magnetocrystalline anisotropy. The complex domain wall

dynamics in complicated multiphase microstructures will bring about more difficulty in revealing the reversal mechanism. In order to accurately capture the domain features by micromagnetic simulations and avoid artificial pinning, the discretization cell size is chosen as 1 nm which is smaller than the domain wall width ($\delta_w = \pi\sqrt{A/K} \sim 5.24 \text{ nm}$) and exchange length ($\delta_{\text{ex}} = \sqrt{2A/\mu_0 M_s^2} \sim 2.77 \text{ nm}$) of $\text{Nd}_2\text{Fe}_{14}\text{B}$ grain. Micromagnetic simulations were carried out by using the 3D NIST OOMMF code.³⁴

III. RESULTS AND DISCUSSION

We first investigated the reversal process in $\text{Nd}_2\text{Fe}_{14}\text{B}$ single grain of different grain shapes, as the results shown in Figs. 2 and 3. The initial magnetization is along the easy axis (z axis here), and an opposite external magnetic field $\mu_0 H_{\text{ex}}$ is applied to switch the whole grain. The distribution of the z component of the unit magnetization vector (m_z) at the remanent state ($\mu_0 H_{\text{ex}} = 0$) is presented in Fig. 2(a). It can be seen that the magnetization near the corners or edges has already rotated out of the easy direction even at the remanent state for the prism grains. More precisely, according to the minimum m_z values in Fig. 2(b), the local reversal happens fast in the prism grains, especially in the triangular prism. This is due to the inhomogeneous stray field near the corners or edges in the nonellipsoidal grains.^{21,22} In contrast, no apparent local reversal occurs in the spheroid grain. By the local reversal, the inhomogeneous magnetization can repress magnetic surface charges and decrease the stray-field energy with respect to the homogeneous magnetic state. But in the

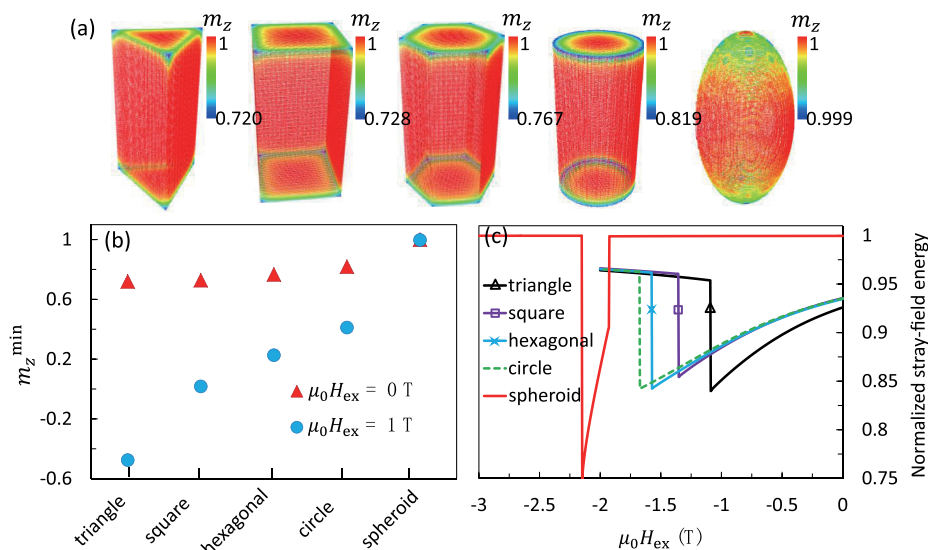


FIG. 2. (a) m_z distribution at the remanent state for $\mu_0 H_{\text{ex}} = 0$. (b) Minimum m_z component at $\mu_0 H_{\text{ex}} = 0$ and 1 T as a function of grain shape. (c) Stray-field energy, normalized to its value in the saturated state, as a function of the external field. $t = 3 \text{ nm}$, $d = 100 \text{ nm}$, and $h = 200 \text{ nm}$.

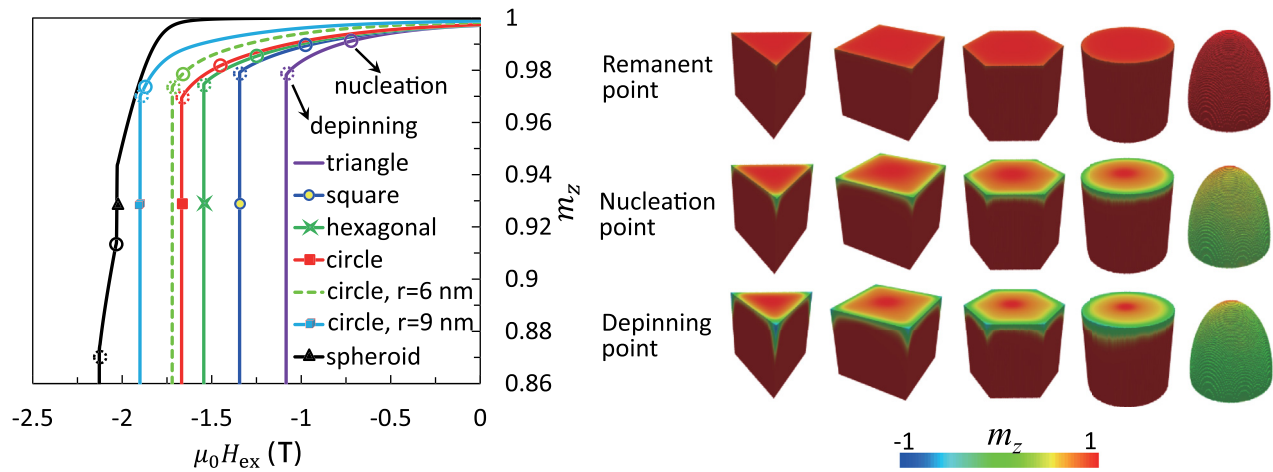


FIG. 3. Reversal process for different grain shapes ($t = 3$ nm, $d = 100$ nm, and $h = 200$ nm) show nucleation and depinning mechanisms. Nucleation point is determined by the formation of at least a 90° domain wall at corners or edges.²⁷ Only half of the model is displayed here. The legends “circle, $r = 6$ nm” and “circle, $r = 9$ nm” denote that the edge of the grain with a circular cross section is rounded by a chamfer with a radius of 6 and 9 nm, respectively.

spheroid grain, both the stray field and magnetization remain uniform until a sufficiently high external field is applied. These different behaviors can also be understood by comparing the reduction of the stray-field energy, as shown in Fig. 2(c). A higher reduction in stray-field energy leads to more inhomogeneous local state for the nucleation. It is apparent that the stray-field energy in the prisms is reduced much faster than that in the spheroid, consistent with the results in Figs. 2(a) and 2(b).

The different local reversal behavior could result in distinct nucleation fields. For the complex system with hard grains and soft defect layers, the nucleation field cannot be determined analytically. Following the idea from the previous work,²⁷ we take the nucleation field $\mu_0 H_n$ to be the field required to flip the polarity of m_z at the grain corners or edges to force the formation of at least a 90° domain wall. The computed reversal processes for all the grain shapes are shown in Fig. 3, in which the nucleation and depinning fields are indicated. In all the prisms local reversal first occurs at the corners and edges, followed by the nucleation of a reversal domain inside the defect layer. For instance, in the triangular prism nucleation happens at $\mu_0 H_n = 0.668$ T. Then the reversal domain expands until an energy barrier is overcome by the depinning field. For the triangular prism, at a depinning field of 1.080 T, the reversal domain rapidly expands and the whole grain is completely reversed instantly. In contrast, due to the uniform stray field along the easy axis, the magnetization in the spheroid grain can be stabilized until a large external field is applied. The difference between the high nucleation field (2.036 T) and the high depinning field (2.128 T) is also small. These results indicate clear nucleation and depinning mechanisms for the reversal process. In addition to the sharp edges in the prisms, we also investigate the effect of smooth edges. Taking the grain with a circular cross section as an example, we smooth the end edge by a chamfer with a radius of 6 and 9 nm. The calculated reversal curves are shown in Fig. 3, as comparisons to the case of sharp edge. The smoothness of the sharp edge reduces

surface charges and lowers the magnetostatic energy, favorable for delaying the nucleation. It can be seen from Fig. 3 that smoothing the edge increases both the nucleation field and coercivity and decrease the difference between them. For example, a 6 and 9 nm chamfer radius can improve the coercivity from 1.67 T to 1.73 T and 1.91 T, respectively. These results are consistent with the previous work.³⁰

The calculated 2nd quadrants of the hysteresis curves are presented in Fig. 4(a). The coercivity in the spheroid is shown to be highest, followed by that in circular prism, in hexagonal prism, in square prism, and in triangular prism, respectively. The coercivity of 2.128 T in the spheroid grain is almost as twice as the coercivity of 1.088 T in the triangular prism. Above discussion has indicated that the grain shape can influence the local reversal behavior and thus the nucleation field and the depinning field. Since the magnetization is inhomogeneous here, the shape anisotropy cannot be well defined theoretically. We turn to the equivalent shape contribution to quantitatively evaluate the role of grain shape on coercivity. It should be noted that it is not easy to define a constant volume when the grain has distinct cross-section geometry. Instead, the same geometry parameters d and height h in Fig. 1 are used for different shaped grains whose volumes are varied. The case of constant volume with different aspect ratios h/d but the same grain shape will be studied in the following. So the equivalent shape contribution discussed in Fig. 4(b) is attributed to a combined effect of the volume and shape. As shown in Fig. 4(b), we fit the normalized coercivity (H_c/M_s) as a function of the normalized anisotropy field ($2K/\mu_0 M_s^2$) by the equation

$$\frac{H_c}{M_s} = \epsilon \frac{2K}{\mu_0 M_s^2} + \epsilon_s, \quad (1)$$

in which ϵ and ϵ_s represent the anisotropy field contribution and shape contribution to the coercivity, respectively. From the fitting parameters listed in Fig. 4(b), it is evident that both ϵ and ϵ_s decrease in the same fashion as the coercivity, i.e., spheroid > circular prism > hexagonal prism > square prism > triangular prism. This indicates that tailoring the

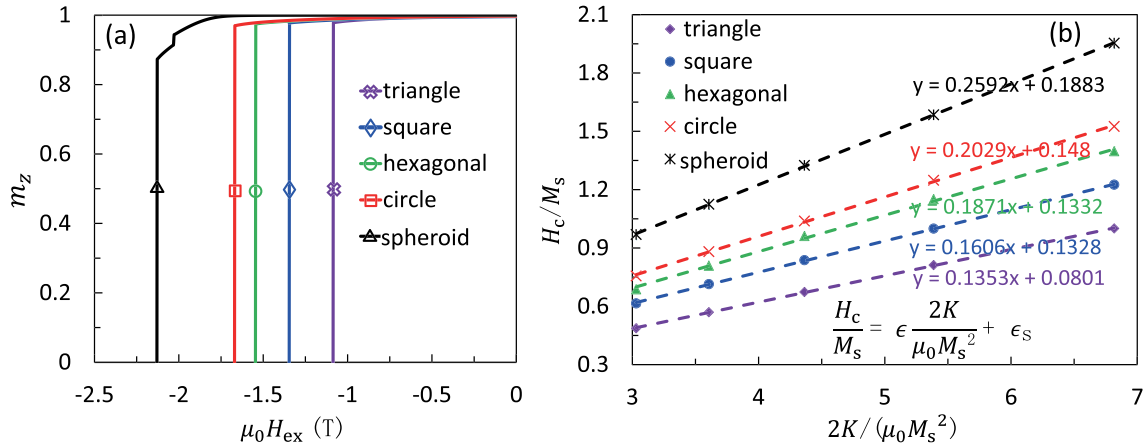


FIG. 4. (a) Simulated reversal curves for spheroid and prisms with various cross sections. (b) The normalized coercivity (H_c/M_s) as a function of the normalized anisotropy field ($2K/\mu_0 M_s^2$). Fitting curves show the anisotropy field contribution (ϵ) and shape contribution (ϵ_s) to the coercivity. $t = 3$ nm, $d = 100$ nm, and $h = 200$ nm.

grain shape cannot only control the shape contribution but also the anisotropy field contribution to the coercivity.

Temperature also affects the coercivity. The temperature dependence of coercivity is generally due to two factors: the temperature-dependent magnetocrystalline anisotropy and the thermal fluctuations at finite temperatures. Bance *et al.* considered both of these two factors in their micromagnetic simulations and found that thermal fluctuations can reduce the coercivity by 15% at room temperature and by 25% at 450 K.^{25,26} Here, the grain shape is the focus and the thermal fluctuations are ignored. We take the temperature dependent magnetocrystalline anisotropy and saturation magnetization³⁷ to simulate the temperature dependence of coercivity, as shown in Fig. 5. Expectedly, the coercivity is found to decrease with temperature. The decreasing trend of all the grains with different shapes is similar. The decrease rate $\kappa = d(\mu_0 H_c)/dT$ is larger at higher temperatures after 400 K. The distinct values of κ before and after 400 K may be attributed to a synergetic effect of the magnetocrystalline anisotropy

and saturation magnetization, both of which decrease with temperature.³⁷ It is found that the grain shape with higher coercivity has a smaller κ and thus is more sensitive to temperature. The underlying reasons should be further explored.

Fig. 6 contains a plot of the computed $\mu_0 H_c$ against the defect thickness (t) for all the grain shapes. The theoretical plot is taken from the Aharoni's 1D defect model.³⁵ In this 1D model, an infinite ferromagnetic material with a soft interface of finite thickness was considered. In all cases, the calculated $\mu_0 H_c$ here is lower than that from the theoretical prediction in which the coercivity value is the upper bound. In contrast to the Aharoni's model which is infinite in size, the real grains and our modelled grains here are of finite size. So the difference between the model and the simulation is expected. But the trend of the coercivity varying with the defect thickness agrees well with the model prediction.

Since the spheroid shape has much higher coercivity, we investigate the effect of aspect ratio (h/d) in the spheroid grain, as shown in Fig. 7. The volume of the spheroid is kept

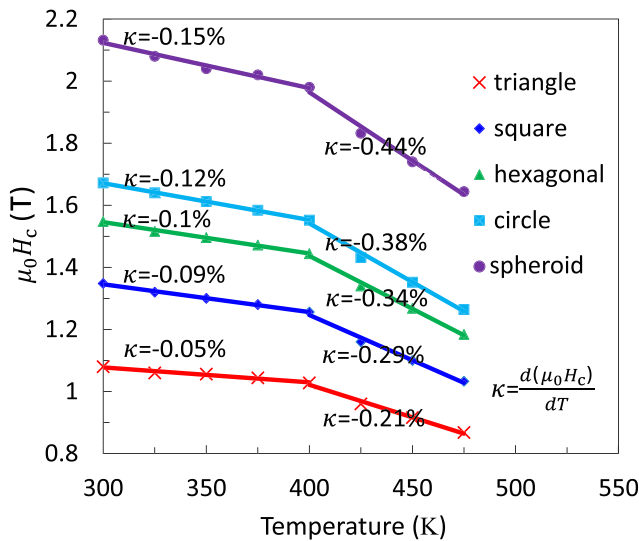


FIG. 5. Simulated temperature-dependent coercivity of grains with different shapes.

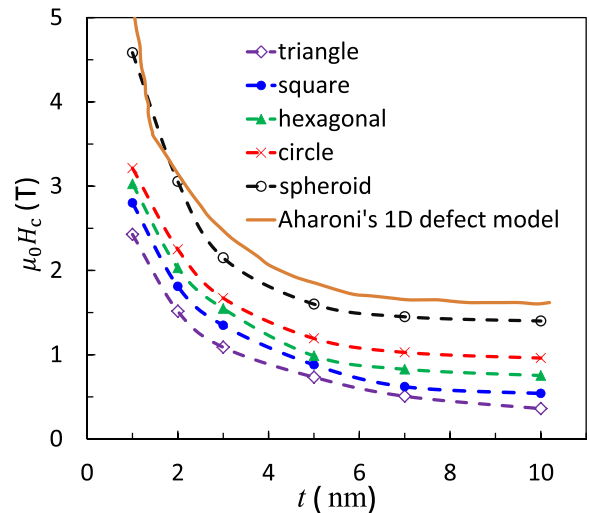


FIG. 6. Dependence of coercivity on the defect thickness t , with theoretical plot from Aharoni's 1D defect model³⁵ of infinite material for comparison. $d = 100$ nm and $h = 200$ nm.

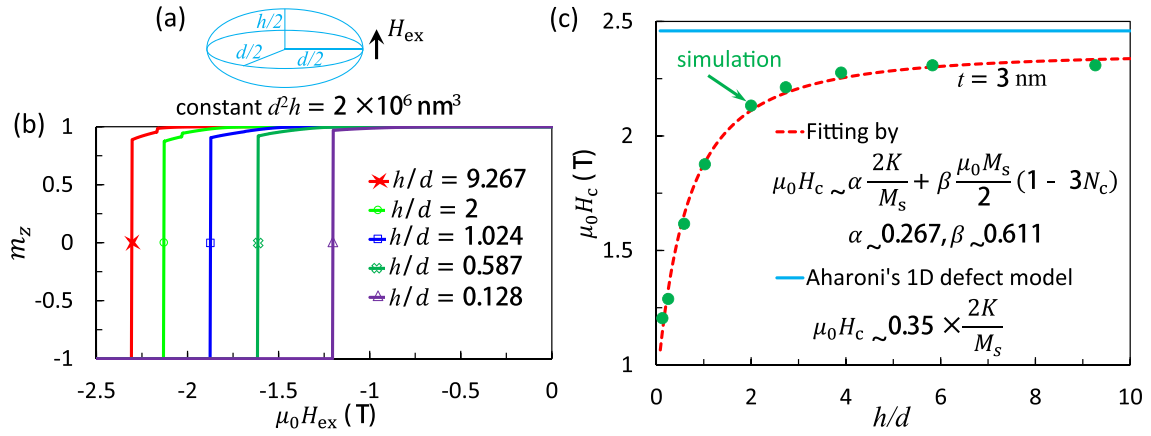


FIG. 7. (a) Schematic of the spheroid. (b) Simulated reversal curves for spheroid with different aspect ratios (h/d). (c) A plot of μ_0H_c against h/d , with Aharoni's 1D defect model³⁵ for comparison. $d = 100$ nm and $h = 200$ nm.

constant with h/d ranging from 0.128 up to 9.267, as schematized in Fig. 7(a). The reversal curves in Fig. 7(b) apparently show the h/d dependent hysteretic behaviors. It should be noted that for the ideal case of coherent magnetization rotation in the spheroid without defects, the additional coercivity due to the shape contribution can be analytically derived as $H_s = 0.5M_s(1 - 3N_c)$.³⁰ N_c is the demagnetizing factor parallel with the easy axis, which can also be analytically calculated as a function of h/d .³⁸ However, the simulated spheroid grain here is covered by a defect layer, and the magnetization rotation is inhomogeneous after a sufficient high magnetic field is reached. So H_s cannot be simply added to the calculated coercivity. Actually, fitting the relationship between the coercivity and h/d leads to an empirical equation

$$\mu_0H_c = \alpha H_A + \beta H_s, \quad (2)$$

in which $\alpha \sim 0.267$ and $\beta \sim 0.611$, as shown in Fig. 7(c). The underlying physical mechanism is that the coercivity is a linear mixture of the anisotropy field $H_A = 2K/M_s$ and the shape contribution H_s . In the ideal case, $\alpha = \beta = 1$. But in the real case, α and β are usually less than 1. In Fig. 7(c), it is also evident that above a h/d of ~ 4 coercivity reaches a plateau which is just below the upper bound predicted from the 1D defect model.³⁵ It should be mentioned that the calculated values of α and β in Fig. 7(c) are only valid for the case of

$t = 3$ nm. α and β are dependent on t . It should also be noted that Eq. (2) for the single grain is different from the case of multigrain, in which the effective demagnetization contribution is subtracted from the anisotropy field contribution.³⁹ In the single grain case, there is no demagnetization field from other grains, while in the multigrain case the additional local demagnetization field from other grains often supports the nucleation and lowers the coercivity.

The $\text{Nd}_2\text{Fe}_{14}\text{B}$ grain with a spheroid shape is seldom reported in experiments, though it has much higher coercivity. In the experimental work, columnar and platelet grains are of interests. For example, columnar grains with a diameter of several hundred nanometers can be prepared by sputtering at suitable temperature.⁴⁰ Platelet grains in the submicrometer scale can be obtained by hot deformation (hot compacting and subsequent die-upsetting) of melt-spun powder.³⁶ Fig. 8 shows the simulation results of the columnar and platelet grains with different cross sections. For each cross-section geometry, the volume is kept constant and only h/d varies. This is consistent with the hot deformation process, in which h/d decreases and the degree of texture is increased when the volume is kept nearly constant. It can be seen from Fig. 8(a) that the coercivity remarkably increases with h/d and then almost saturates around $h/d \sim 4$. The m_z distribution at the depinning point in Fig. 8(b) also presents the h/d dependent reversal characteristics. In the extremely

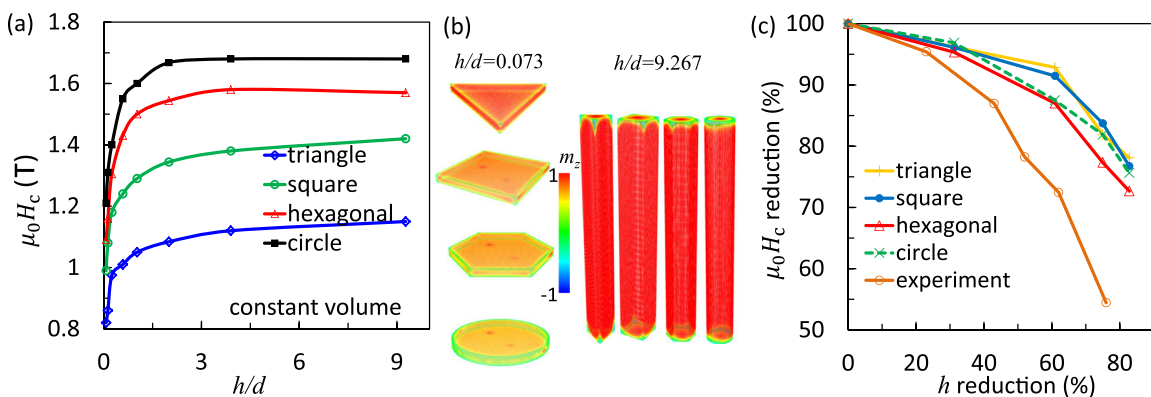


FIG. 8. (a) A plot of μ_0H_c against h/d for different grain shapes, with constant $d^2h = 2 \times 10^6$ nm³. (b) m_z distribution of different grains at the depinning point. (c) Coercivity reduction as a function of height reduction. The experimental results are taken from Ref. 36. $t = 3$ nm.

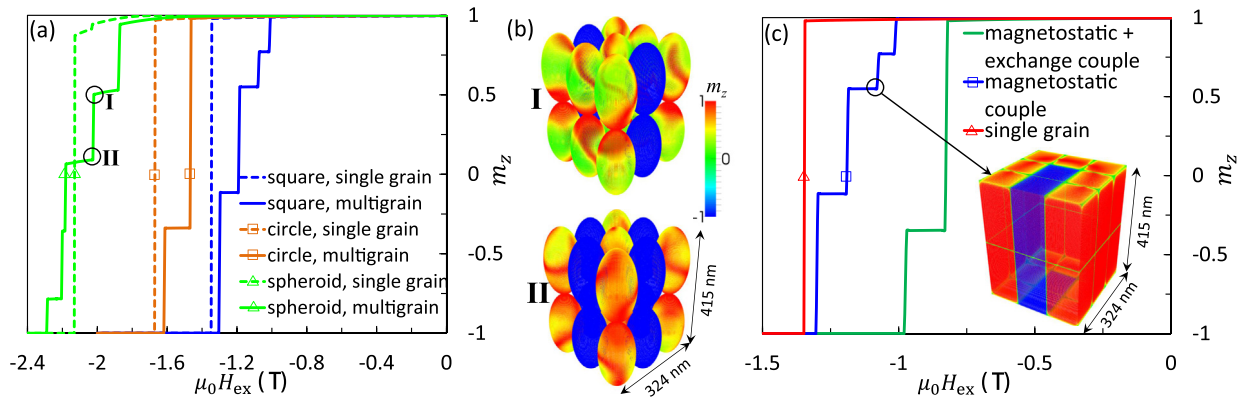


FIG. 9. Simulated reversal curves for multigrains with (a) only magnetostatic coupling and (c) both magnetostatic and exchange couplings. (b) Contours for magnetization state at points I and II in (a). $h/d=2$ in the individual grain. $t=3$ nm. The legend “single grain” indicates the reversal curve for a single grain, not for the uncoupled grains.

flat platelet grain (e.g., $h/d=0.073$), the whole grain has been partially reversed at the depinning point. But in the columnar grain (e.g., $h/d=9.267$), only the edges or corners at the two ends are partially reversed. This distinct feature can be attributed to the grain shape; because the platelet and columnar grains favor an in-plane and out-of-plane magnetization distribution, respectively. We also take the experimental results for comparison,³⁶ as shown in Fig. 8(c). According to the experiment,³⁶ the initial h is chosen such that $h/d=1$. The h reduction is defined by subtracting the ratio of the final h to the initial h from unity. The simulated decreasing trend of the coercivity reduction varying with h reduction accords with the experimental trend. The coercivity is reduced more slowly in the simulation than in the experiment. This discrepancy could be owing to two reasons. First, the simulated sample is single grain and its size is much smaller than the experimental size so that the stray field effect is not fully considered. Indeed, Bance *et al.*²⁴ have demonstrated that smaller grain size leads to a smaller demagnetizing factor and thus a higher coercivity. Second, the degree of texture varies with h reduction in the experiment but ignored in the simulation.

We further assemble eighteen grains ($h/d=2$) into multigrain models (Fig. 9), in order to elucidate the effect of magnetostatic or exchange coupling. Fig. 9(a) compares the hysteresis curves of individual grains and magnetostatically

coupled multigrains. In the multigrain, nonmagnetic materials are set between two neighbor grains so that exchange coupling vanishes. The simulated box is with a size of $324 \times 324 \times 415$ nm³, which is meshed into nearly 44×10^6 cells and is computationally expensive. Due to the limited number of grains in the multigrain model, the hysteresis curves exhibit a step-like behavior. This is related to the intermittent switching of several or individual grains, as evidenced in the magnetization distribution during the switching process (Fig. 9(b)). More importantly, from Fig. 9(a) we can calculate that the nucleation field is reduced by $\sim 14\%$ – 30% and the coercivity by $\sim 10\%$ if the magnetostatic coupling is included. Furthermore, if both the magnetostatic and exchange couplings are included, the coercivity is further reduced by $\sim 40\%$, as shown in Fig. 9(c). In addition, Fig. 10 contains the results on multigrains constituted by platelet and columnar grains which are magnetostatically coupled. In the case of platelet grains (Figs. 10(a) and 10(b)), the coercivity reduction by the magnetostatic coupling in the grain with a square cross section is $\sim 45\%$, much larger than that in a circular cross section ($\sim 10\%$). This indicates that the circular cross section of individual grains is favorable for weakening the magnetostatic coupling and enhancing the coercivity in multigrains constituted by platelet grains. In contrast, for the columnar multigrains the magnetostatic coupling reduces the coercivity by $\sim 10\%$ both in the square and circular cross sections. But the circular cross

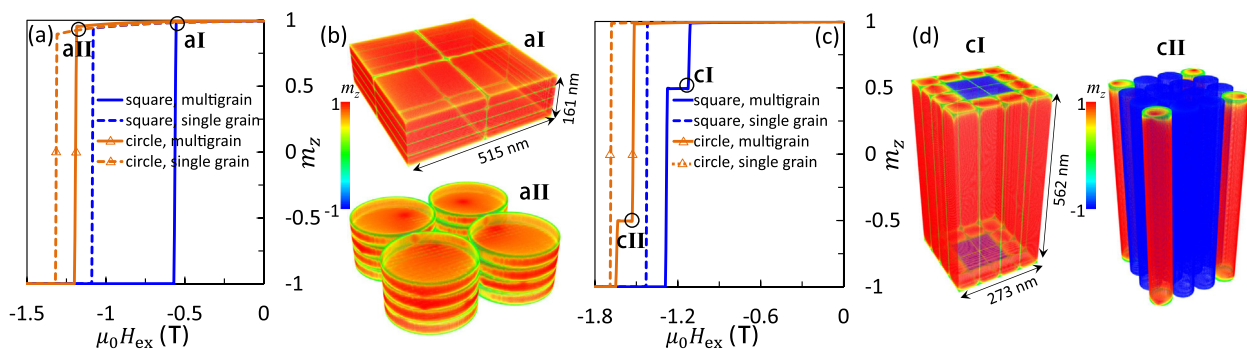


FIG. 10. Simulated reversal curves and magnetization distribution for magnetostatically coupled multigrains constituted by (a), (b) platelet grains ($h/d=0.128$) and (c) and (d) columnar grains ($h/d=9.267$). $t=3$ nm. The legend “single grain” indicates the reversal curve for a single grain, not for the uncoupled grains.

section can result in higher coercivity. These results based on the multigrain models, especially in the case of platelet and columnar grains, indicate the possibility to enhance the coercivity by controlling the grain shape in the real multigrain samples.

IV. CONCLUSIONS

The spheroid grain and the prism grains with circular, hexagonal, square, and triangular cross sections were studied to demonstrate the effect of grain shape and defect layer in Nd-Fe-B magnets. The trend of coercivity varying with defect thickness was shown to be consistent with the 1D defect model whose coercivity value is the upper bound. By adjusting the distinct anisotropy field contribution and shape contribution, we were able to increase the coercivity by a factor of ~ 2 through the change of grain shape from the triangular prism to the spheroid. The coercivity, along with both the anisotropy field contribution and the shape contribution, was found to decrease in the order: spheroid > circular prism > hexagonal prism > square prism > triangular prism. In terms of sputtered columnar grains and hot-deformed platelet grains in the submicrometer scale, simulations of differently shaped grains with a constant volume and varied aspect ratios indicated that the coercivity enhancement nearly plateaus above an aspect ratio of ~ 4 . Multigrain ensembles containing above-mentioned single grains were further simulated, showing that the magnetostatic coupling among grains further reduce the coercivity by $\sim 10\%$ – 45% when compared to the case of single grain. This simulation work could provide useful information on tailoring the grain shape to improve the coercivity in Nd-Fe-B magnets.

ACKNOWLEDGMENTS

The support from the German federal state of Hessen through its excellence programme LOEWE “RESPONSE” and the Lichtenberg High Performance Computer of TU Darmstadt is acknowledged.

- ¹O. Gutfleisch, M. A. Willard, E. Brück, C. H. Chen, S. Sankar, and J. P. Liu, *Adv. Mater.* **23**, 821 (2011).
- ²T. Woodcock, Y. Zhang, G. Hrkac, G. Ciuta, N. Dempsey, T. Schrefl, O. Gutfleisch, and D. Givord, *Scr. Mater.* **67**, 536 (2012).
- ³M. Ghandehari, *Appl. Phys. Lett.* **48**, 548 (1986).
- ⁴C. De Groot, K. Buschow, F. De Boer, and K. de Kort, *J. Appl. Phys.* **83**, 388 (1998).
- ⁵M. Sagawa, S. Hirosawa, K. Tokuhara, H. Yamamoto, S. Fujimura, Y. Tsubokawa, and R. Shimizu, *J. Appl. Phys.* **61**, 3559 (1987).
- ⁶K. Löewe, C. Brombacher, M. Katter, and O. Gutfleisch, *Acta Mater.* **83**, 248 (2015).

- ⁷S. Sawatzki, I. Dirba, H. Wendrock, L. Schultz, and O. Gutfleisch, *J. Magn. Magn. Mater.* **358**, 163 (2014).
- ⁸S. Sawatzki, I. Dirba, L. Schultz, and O. Gutfleisch, *J. Appl. Phys.* **114**, 133902 (2013).
- ⁹J. Fidler and T. Schrefl, *J. Appl. Phys.* **79**, 5029 (1996).
- ¹⁰J. Fidler and T. Schrefl, *J. Phys. D: Appl. Phys.* **33**, R135 (2000).
- ¹¹M. Yi, B.-X. Xu, and D. Gross, *Mech. Mater.* **87**, 40 (2015).
- ¹²M. Yi, B.-X. Xu, and Z. Shen, *Extreme Mech. Lett.* **3**, 66 (2015).
- ¹³M. Yi, B.-X. Xu, and Z. Shen, *J. Appl. Phys.* **117**, 103905 (2015).
- ¹⁴M. Yi and B.-X. Xu, *Proc. R. Soc. A* **470**, 20140517 (2014).
- ¹⁵H. Sepehri-Amin, T. Ohkubo, M. Gruber, T. Schrefl, and K. Hono, *Scr. Mater.* **89**, 29 (2014).
- ¹⁶J. Liu, H. Sepehri-Amin, T. Ohkubo, K. Hioki, A. Hattori, T. Schrefl, and K. Hono, *Acta Mater.* **82**, 336 (2015).
- ¹⁷G. Hrkac, K. Butler, T. Woodcock, L. Saharan, T. Schrefl, and O. Gutfleisch, *JOM* **66**, 1138 (2014).
- ¹⁸G. Hrkac, T. Woodcock, K. Butler, L. Saharan, M. Bryan, T. Schrefl, and O. Gutfleisch, *Scr. Mater.* **70**, 35 (2014).
- ¹⁹G. Hrkac, T. G. Woodcock, C. Freeman, A. Goncharov, J. Dean, T. Schrefl, and O. Gutfleisch, *Appl. Phys. Lett.* **97**, 232511 (2010).
- ²⁰J. Fujisaki, A. Furuya, Y. Uehara, K. Shimizu, H. Oshima, T. Ohkubo, S. Hirosawa, and K. Hono, *IEEE Trans. Magn.* **50**, 1 (2014).
- ²¹W. Rave, K. Ramstöck, and A. Hubert, *J. Magn. Magn. Mater.* **183**, 329 (1998).
- ²²T. Schrefl, J. Fidler, and H. Kronmüller, *J. Magn. Magn. Mater.* **138**, 15 (1994).
- ²³J. Thielsch, D. Suess, L. Schultz, and O. Gutfleisch, *J. Appl. Phys.* **114**, 223909 (2013).
- ²⁴S. Bance, B. Seebacher, T. Schrefl, L. Exl, M. Winklhofer, G. Hrkac, G. Zimanyi, T. Shoji, M. Yano, N. Sakuma *et al.*, *J. Appl. Phys.* **116**, 233903 (2014).
- ²⁵S. Bance, J. Fischbacher, A. Kovacs, H. Oezelt, F. Reichel, and T. Schrefl, *JOM* **67**, 1350 (2015).
- ²⁶S. Bance, J. Fischbacher, and T. Schrefl, *J. Appl. Phys.* **117**, 17A733 (2015).
- ²⁷S. Bance, H. Oezelt, T. Schrefl, G. Ciuta, N. Dempsey, D. Givord, M. Winklhofer, G. Hrkac, G. Zimanyi, O. Gutfleisch *et al.*, *Appl. Phys. Lett.* **104**, 182408 (2014).
- ²⁸P. Krone, D. Makarov, M. Albrecht, T. Schrefl, and D. Suess, *J. Magn. Magn. Mater.* **322**, 3771 (2010).
- ²⁹J. Fischbacher, S. Bance, M. Gusenbauer, A. Kovacs, H. Oezelt, F. Reichel, and T. Schrefl, in Proceedings of the 23rd International Workshop on Rare Earth and Future Permanent Magnets and Their Applications (REPM2014) (Annapolis, Maryland, USA, 2014).
- ³⁰S. Bance, J. Fischbacher, T. Schrefl, I. Zins, G. Rieger, and C. Cassignol, *J. Magn. Magn. Mater.* **363**, 121 (2014).
- ³¹H. Sepehri-Amin, T. Ohkubo, and K. Hono, *Acta Mater.* **61**, 1982 (2013).
- ³²J. Livingston, *J. Appl. Phys.* **57**, 4137 (1985).
- ³³K.-D. Durst and H. Kronmüller, *J. Magn. Magn. Mater.* **59**, 86 (1986).
- ³⁴M. J. Donahue and D. G. Porter, *OOMMF Software Package*, <http://math.nist.gov/oommf>.
- ³⁵A. Aharoni, *Phys. Rev.* **119**, 127 (1960).
- ³⁶K. Khlopkov, O. Gutfleisch, D. Hinz, K.-H. Müller, and L. Schultz, *J. Appl. Phys.* **102**, 023912 (2007).
- ³⁷M. Sagawa, S. Fujimura, H. Yamamoto, Y. Matsuura, and S. Hirosawa, *J. Appl. Phys.* **57**, 4094 (1985).
- ³⁸J. Osborn, *Phys. Rev.* **67**, 351 (1945).
- ³⁹K.-D. Durst and H. Kronmüller, *J. Magn. Magn. Mater.* **68**, 63 (1987).
- ⁴⁰N. M. Dempsey, A. Walther, F. May, D. Givord, K. Khlopkov, and O. Gutfleisch, *Appl. Phys. Lett.* **90**, 092509 (2007).